SCIENCE CHINA
Chemistry

•ARTICLES•

https://doi.org/10.1007/s11426-024-2198-9

Pyrrolic nitrogen coordinated Ni^{2+} dual-atom catalyst for boosting CO_2 electroreduction

Zhi-Wei Chen[†], Hong-Juan Wang[†], Chang Liu, Xiu-Li Lu & Tong-Bu Lu[*]

MOE International Joint Laboratory of Materials Microstructure, Institute for New Energy Materials and Low Carbon Technologies, School of Materials Science and Engineering, Tianjin University of Technology, Tianjin 300384, China

Received May 26, 2024; accepted July 9, 2024; published online October 14, 2024

Nitrogen-doped carbon materials have been widely used for the constructions of single-atom catalysts, while the effect of different species of doped nitrogen on the catalytic activity of CO_2 electroreduction has rarely been investigated. Here we found that pyrrolic-N coordinated Ni^{2+} catalysts display much higher electrocatalytic CO_2-to-CO activity and selectivity than the corresponding pyridinic-N coordinated low valent $Ni^{(0\sim+2)}$ catalysts, and pyrrolic-N coordinated Ni_2 dual-atoms catalyst of Ni_2/N-CNTs exhibits the best electrocatalytic performance, with over 90% Faradaic efficiencies in a broad potentials from −0.6 to −1.2 V vs. reversible hydrogen electrode, as well as an outstanding CO specific current of 56.2 A/mg_{Ni} and high turnover frequency of 6.2×10^4 h^{-1}, over 7-times higher than those of pyridinic-N coordinated Ni catalysts. Electrochemical results indicate the weak electron-donor nature of pyrrolic-N facilitates the generation of a reduced active site at low overpotential for boosting CO_2 electroreduction. Density functional theory calculations reveal that the reaction free energy for the *COOH formation on pyrrolic-N coordinated Ni catalysts are lower than those on pyridinic-N coordinated Ni catalysts, and a H_2O-adsorbed Ni_2/N-CNTs displays the optimized reaction free energy for both *COOH formation and CO desorption, which derive the best catalytic performance.

dual-atom catalyst, CO_2 electroreduction, synergistic catalysis, pyrrolic-N, pyridinic-N

Citation: Chen ZW, Wang HJ, Liu C, Lu XL, Lu TB. Pyrrolic nitrogen coordinated Ni^{2+} dual-atom catalyst for boosting CO_2 electroreduction. *Sci China Chem*, 2024, 67, https://doi.org/10.1007/s11426-024-2198-9

1 Introduction

Electrochemical reduction of CO_2 to fuels and chemicals using clean and renewable electricity generated by solar or wind energy is a promising way to address the global warming and energy shortage [1–6]. However, the development of electrocatalysts for highly efficient and selective reduction of CO_2 to a particular product remains challenge due to the kinetic inertness, the multiple proton coupled electron transfer process, and the competitive hydrogen evolution reactions (HER) [7–10]. Recently, single atom catalysts (SACs) have been intensively investigated for electrochemical reduction of CO_2 due to their certain active sites and nearly 100% metal utilization, with impressive activity and selectivity [11–14], in which N-doped carbon (N-C) anchored SACs (M-N-C) have been drawn particular attention for their facile synthesis and structural characterization, high catalytic activity and stability, and understandable structure-activity relationship [15–17]. Never the less, the effect of different species of doped nitrogen on the catalytic activity of CO_2 electroreduction has rarely been investigated [13].

As CO_2 electroreduction involves multi-step reactions, the catalytic performance of SACs usually suffers from the high reaction free energies of a given step [18]. For instance, the catalytic activity of Ni-N_4 SAC for electroreduction CO_2 to CO is limited by the high reaction free energy for the for-

†Equally contributed to this work.
*Corresponding author (email: lutongbu@tjut.edu.cn)

mation of *COOH intermediate on Ni site (* denotes the adsorption site) [19,20], while the catalytic activity of Fe-N_4 SAC is restricted by the hard *CO desorption on Fe site [13,21]. These limitations can be attributed to the simplicity of the single catalytic site, which can only be favorable to catalyze single-molecule elementary reactions [22,23]. In contrast to SACs, introducing a second metal atom to adjacent position of the single-metal site to construct dual-atom catalysts (DACs) can break the above limitations of SACs. Generally, DACs can achieve higher catalytic performance than SACs, as two adjacent metal sites can generate a synergistic catalysis for a multi-steps and multi-intermediate reaction, such as CO_2 electroreduction [23–28]. For example, we found that the catalytic activity and selectivity for photocatalytic CO_2 to CO by dinuclear metal complex are much higher than those of corresponding mononuclear complex due to the synergistic catalysis effect between two adjacent metal atoms, in which one metal ion serves as the catalytic site and the other metal ion acts as the assistant catalytic site to promote the cleavage of C–OH bond of O=C–OH intermediate [29,30]. However, controlled syntheses of DACs with suitable M–M distance remain great challenge. Though the methods of atomic-layer deposition and impregnation-adsorption can precisely fabricate dual-metal sites on the supports, the stability of as-prepared DACs is usually poor due to the weak interactions between the dual-metal sites and support [31]. The pyrolysis and post acid treatment of mixed metal salts with N-doped carbon materials is the most common approach for the synthesis of DACs [20,26,32–34], while this will inevitably lead to the formation of a mixture of DACs and SACs.

We try to use stable dinuclear Ni_2L_2 complex (L = 4-amino-3,5-di-2-pyridyl-4*H*-1,2,4-triazole) and oxidized carbon nanotubes (O-CNTs) as precursors for precisely controlled synthesis of Ni_2 DACs. In comparison to conventional one-pot synthesis method of pyrolysis and post acid treatment, which will inevitably generate a mixture of SAC, DAC, and metal nanoparticles, our synthesis strategy can produce DACs with high purity, as the predecessor we used is a stable dinuclear metal complex (up to 300 °C), thus Ni_2 pair in Ni_2L_2 has more opportunity to be bound together during the pyrolysis process to get pure DACs. Benefiting from the tightly bound Ni_2 site by the ligand, the pyrolysis of stable Ni_2L_2 complex with O-CNTs and dicyandiamide at 500 °C generates a Ni_2/N-CNTs DAC (N-CNTs = N-doped CNTs). Unexpectedly, we found that pyrrolic-N coordinated isolated Ni^{2+} dual-atom sites were *in-situ* generated in Ni_2/N-CNTs DAC. For comparison, Ni/N-CNTs SAC was also synthesized using the same procedure as Ni_2/N-CNTs DAC, except using mononuclear NiL_2 to instead of dinuclear Ni_2 L_2. Interestingly, when the pyrolysis temperature was increased to 1000 °C, we found that pyrrolic-N coordinated Ni_2/N-CNTs and Ni/N-CNTs transfer to pyridinic-N coordinated Ni_2/N-CNTs-1000 and Ni/N-CNTs-1000, respectively. The results of electrochemical measurements show that Ni_2/N-CNTs display the best CO_2-to-CO electrocatalytic performance, with a j_{CO} mass activity of 56.2 A/mg_{Ni}, 2.7, 7.1 and 8.3-times more active than those Ni/N-CNTs, Ni_2/N-CNTs-1000 and Ni/N-CNTs-1000, respectively. Electrochemical measurements indicate the CO_2 reduction potentials of Ni_2/N-CNTs and Ni/N-CNTs are lower than those of Ni_2/N-CNTs-1000 and Ni/N-CNTs-1000. Density functional theory (DFT) calculations reveal that the formation free energy for the rate-limiting step of *COOH on dual Ni_2 site in Ni_2/N-CNTs is lower than those on single Ni site in Ni/N-CNTs and Ni/N-CNTs-1000, and thus displays superior performance for electroreduction of CO_2 to CO.

2 Experimental

2.1 Materials

The ligand 4-amino-3,5-di-2-pyridyl-4*H*-1,2,4-triazole was synthesized according to the literature [35]. $NiCl_2·6H_2O$, $Ni(NO_3)_2·6H_2O$, and multi-wall CNTs were purchased from Aladdin (China). Nafion perfluorinated resin solution (5 wt% in lower aliphatic alcohols and water, containing 15%–20% water) was purchased from Sigma-Aldrich. All other chemicals were commercially available and used directly without further purification.

2.2 Material synthesis

Synthesis of mononuclear **NiL_2** complex. A methanol solution (15 mL) of $Ni(NO_3)_2·6H_2O$ (0.58 g, 2 mmol) was added dropwise to a stirred solution of 4-amino-3,5-bis-(2-pyridyl)-1,2,4-triazole (abpt, 0.48 g, 2 mmol) in 15 mL methanol. After 2 h, the light purple precipitate was formed. It was collected by filtration, followed by washing with diethyl ether. The mother liquor of methanol was evaporated slowly in the air to get purple crystals.

Synthesis of dinuclear **Ni_2L_2** complex. A solution of abpt (0.72 g, 3 mmol) in warm ethanol (30 mL) was added dropwise to a solution of $NiCl_2·6H_2O$ (0.71 g, 3 mmol) in water (15 mL). Light blue crystals were formed on standing the solution for several hours. The crystals were isolated by filtration.

Synthesis of **O-CNTs**. To oxidize and remove any metal impurity in CNTs, CNTs was added to concentrated nitric acid, and heated at 120 °C for 10 h. It was separated by centrifugation, and washed several time with water to neutral.

Synthesis of **Ni_2/N-CNTs**. A mixture of as-prepared Ni_2L_2 (3.6 mg) and oxidized CNTs (100 mg) was dispersed in 50 mL MeOH, and stirred at room temperature for 12 h. Then the methanol solvent was removed by rotary evaporation to get a mixture of Ni_2L_2/O-CNTs. Afterwards, 0.1 g of the above Ni_2L_2/O-CNTs mixture and 1 g of dicyandiamide were placed in two separated small porcelain boats within a big porcelain boat covered with a lid. The porcelain boat was heated to 500 °C under Ar atmosphere with a heating rate of 2 °C min^{-1}, and keep at 500 °C for 2 h in a tube furnace to yield Ni_2/N-CNTs. The result of inductively coupled plasma mass spectrometry (ICP-MS) measurement indicates 0.23 wt% of Ni contains in Ni_2/N-CNTs.

Synthesis of **Ni/N-CNTs**. The synthesis process of Ni/N-CNTs is similar to that of Ni_2/N-CNTs except using NiL_2 to replace Ni_2L_2. The result of ICP-MS measurement indicates 0.31 wt% of Ni contains in Ni/N-CNTs.

Synthesis of **Ni_2/N-CNTs-1000**. The synthesis process of Ni_2/N-CNTs is similar to that of Ni_2/N-CNTs except that the temperature was raised to 1000 °C. The result of ICP-MS measurement indicates 0.28 wt% of Ni contains in Ni/N-CNTs-1000.

Synthesis of **Ni/N-CNTs-1000**. The synthesis process of Ni/N-CNTs is similar to that of Ni/N-CNTs except that the temperature was raised to 1000 °C. The result of ICP-MS measurement indicates 0.25 wt% of Ni contains in Ni/N-CNTs-1000.

Synthesis of **N-CNTs**. The synthesis process is similar to that of Ni_2/N-CNTs except the absence of Ni_2L_2.

3 Results and discussion

The dinuclear Ni_2L_2 complex was prepared according to the literature method [36]. The crystals of mononuclear NiL_2 were obtained in methanol solution (Supporting Information online), and its structure was determined by the single crystal X-ray diffraction (Table S1 and Figure S1, Supporting Information online). The results of powder X-ray diffraction (XRD) demonstrate that Ni_2L_2 and NiL_2 were successfully synthesized (Figure S2). The Ni_2/N-CNTs and Ni/N-CNTs were synthesized by pyrolyzing a mixture of Ni_2L_2 or NiL_2 with O-CNTs in the presence of dicyandiamide at 500 °C for 2 h under Ar atmosphere. The detail synthesis procedures were given in the Supporting Information. The as-prepared Ni_2/N-CNTs and Ni/N-CNTs can be used directly as the catalysts for CO_2 electroreduction, without the commonly required post acid treatment to remove the formed metal nanoparticles, indicating using Ni_2L_2 and NiL_2 complexes instead of Ni salt as precursors can efficiently prevent the aggregation of Ni atoms to form Ni nanoparticles during the pyrolysis process. For comparison, Ni_2/N-CNTs-1000 and Ni/N-CNTs-1000 were also synthesized using the same procedures as those of Ni_2/N-CNTs and Ni/N-CNTs, expect the pyrolysis temperature was increased to 1000 °C.

The XRD patterns of Ni_2/N-CNTs, Ni/N-CNTs, Ni_2/N-CNTs-1000, Ni/N-CNTs-1000, and N-CNTs show three peaks at 26.4° 43.0° and 54.5°, respectively (Figure S3), corresponding to the (002), (100), and (004) planes of CNTs [37]. No additional peaks belonging to Ni nanoparticles were observed, implying the Ni atoms might be atom dispersed in Ni_2/N-CNTs, Ni/N-CNTs, Ni_2/N-CNTs-1000, and Ni/N-CNTs-1000. The results of ICP-MS measurements indicate that 0.23, 0.31, 0.28 and 0.25 wt% of Ni were contained in Ni_2/N-CNTs, Ni/N-CNTs, Ni_2/N-CNTs-1000, and Ni/N-CNTs-1000, respectively. Raman spectra of Ni_2/N-CNTs, Ni/N-CNTs, Ni_2/N-CNTs-1000, Ni/N-CNTs-1000 and N-CNTs display two main peaks at 1350 and 1580 cm^{-1} (Figure S4), corresponding to the D and G bands from the disorder-induced C–C vibration and the tangential E_{2g} sp^2 bonded C=C stretching vibration, respectively [38]. The values of I_D/I_G for Ni_2/N-CNTs, Ni/N-CNTs, Ni_2/N-CNTs-1000, and Ni/N-CNTs-1000 are higher than that of N-CNTs, indicating more defects existing in four catalysts due to the coordination between Ni and N doped carbon nanotubes [33]. The morphology of the catalysts was investigated by scanning electron microscopy (SEM) and transmission electron microscopy (TEM). The SEM and TEM images show that all Ni_2/N-CNTs, Ni/N-CNTs, Ni_2/N-CNTs-1000, Ni/N-CNTs-1000, and N-CNTs remain the original carbon nanotubes structure (Figure 1a, e and Figures S5–S8). The high-angle annular dark field scanning transmission electron microscopy (HAADF-STEM) show that no Ni nanoparticles were observed in Ni_2/N-CNTs, Ni/N-CNTs, Ni_2/N-CNTs-1000 and Ni/N-CNTs-1000 (Figure 1b, f and Figures S7c and S8c), which is in good agreement with the results of XRD measurements. The strong Ni–N interaction on the surface of N-CNTs-1000 can prevent the Ni atoms aggregation to lead to the formation of isolated Ni single atoms rather than the Ni nanoparticles during the high-temperature pyrolysis of Ni_2/N-CNTs.

The isolated Ni_2 dual-metal pairs in Ni_2/N-CNTs were confirmed by HAADF-STEM measurement. As shown in Figure 1b, the isolated Ni_2 pairs marked with red circles can be observed in Ni_2/N-CNTs. Statistical analysis on the Ni–Ni distances within isolated Ni_2 pairs indicates that almost all of the Ni atoms appear as Ni_2 dual-atom pairs, with the distances of 2.3–2.5 Å (Figure 1c). The uniform Ni–Ni distances in Ni_2/N-CNTs indicate highly purified Ni_2 dual-metal pairs exist in Ni_2/N-CNTs. These distances are shorter than those of ~3 Å in an μ-O-bridged Ir_2 DAC [39], and 2.9 Å in a recently reported Ni_2/NC DAC consisting of two Ni_1-N_4 sites shared with two bridged nitrogen atoms [31], indicating Ni_2 atom pair in Ni_2/N-CNTs is directly bonded. In contrast to Ni_2/N-CNTs, the HAADF-STEM image of Ni_2/N-CNTs-1000 shows that most of Ni_2 dual-atom pairs in Ni_2/N-CNTs transform to isolated Ni single atoms at 1000 °C (Figure S7c). Similar phenomenon has also been observed in previous report, in which Pt nanoparticles transform to isolated

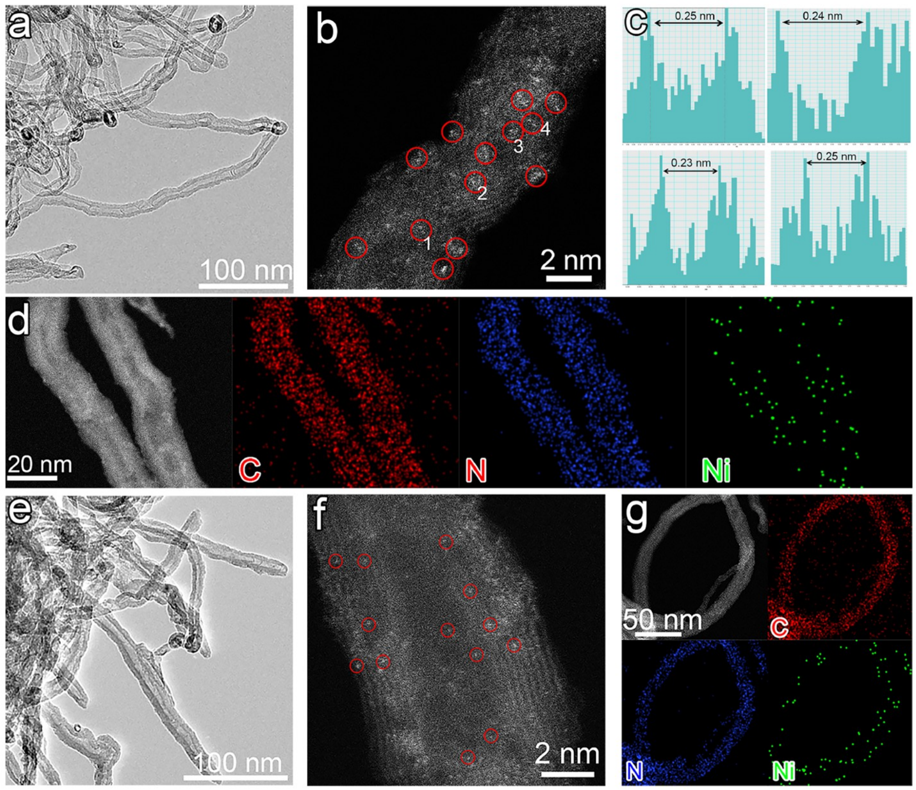

Figure 1 (Color online) (a) TEM image of Ni_2/N-CNTs. (b) HAADF-STEM image of Ni_2/N-CNTs. (c) Intensity profiles of Ni_2 sites in (b). (d) HAADF-STEM image and corresponding element mappings of C, N and Ni for Ni_2/N-CNTs. (e) TEM image of Ni/N-CNTs. (f) HAADF-STEM image of Ni/N-CNTs. (g) HAADF-STEM image and corresponding element mappings of C, N and Ni for Ni/N-CNTs.

Pt atoms at 800 °C due to a strong metal-support interaction [40]. In addition, single bright dots belonging to isolated Ni single atoms were also observed in the HAADF-STEM images of Ni/N-CNTs and Ni/N-CNTs-1000 (Figure 1f and Figure S8c). The energy-dispersive X-ray spectroscopic (EDS) element mappings show that C, N and Ni were all homogeneously distributed over the CNTs in Ni_2/N-CNTs, Ni/N-CNTs Ni_2/N-CNTs-1000, and Ni/N-CNTs-1000 (Figure 1d, g and Figures S7d and S8d).

The X-ray photoelectron spectroscopy (XPS) was conducted to determine the electronic structures and chemical composition of the catalysts. As shown in Figure S9, the peaks of Ni $2p_{3/2}$ binding energy locate at 855.9 and 856.0 eV in Ni_2/N-CNTs and Ni/N-CNTs, respectively. These values are almost the same as that of Ni^{2+} in nickel phthalocyanine (NiPc) (856.0 eV) [19], indicating the valence state of Ni in both Ni_2/N-CNTs and Ni/N-CNTs is Ni^{2+}. In contrast, the peaks of Ni $2p_{3/2}$ binding energies move to 855.3 eV in Ni_2/N-CNTs-1000 and Ni/N-CNTs-1000, indicating the valence state of Ni is between 0 and +2, which is lower than that in Ni_2/N-CNTs and Ni/N-CNTs. No peaks belonging to metallic Ni (853.5 eV) were observed, further demonstrating the absence of Ni nanoparticles in four catalysts. The N 1s in both Ni_2/N-CNTs and Ni/N-CNTs can be deconvoluted into four peaks of pyridinic-N (398.8 eV), pyrrolic-N (400.2 eV), Ni–N (400.6 eV), and graphitic N (401.7 eV), respectively (Figure 2a) [41–43]. The binding energy of pyrrolic-N increased from 400.2 eV in N-CNTs to 400.6 eV in Ni_2/N-CNTs and Ni/N-CNTs (Figure 2a), and the peak position of Ni–N is the same as that in NiPc [44] (Figure S10), demonstrating that the Ni atoms in Ni_2/N-CNTs and Ni/N-CNTs are coordinated to pyrrolic-N rather than pyridinic-N. In contrast, the N 1s in Ni_2/N-CNTs-1000 and Ni/N-CNTs-1000 can be deconvoluted into five peaks of pyridinic-N (398.6 eV), Ni–N (399.6 eV), pyrrolic-N (400.5 eV), graphitic N (401.8 eV), and oxidized N (403.3 eV), respectively (Figure S11), in which the peak position of Ni–N moved from 400.6 eV ($Ni–N_{pyrrolic}$) in Ni_2/N-CNTs and Ni/N-CNTs to 399.6 eV ($Ni–N_{pyridinic}$) in Ni_2/N-CNTs-1000 and Ni/N-CNTs-1000, demonstrating the coordinated N atoms to Ni transformed from pyrrolic-N to pyridinic-N.

X-ray absorption spectroscopy (XAS) was conducted to further investigate the electronic and structural information of Ni atoms in Ni_2/N-CNTs, Ni/N-CNTs, Ni_2/N-CNTs-1000 and Ni/N-CNTs-1000. As shown in the X-ray absorption near-edge structure (XANES) profiles (Figure 2b), the positions of the absorption threshold for Ni_2/N-CNTs and Ni/N-CNTs are close to those of NiO and NiPc, and much higher than that of Ni foil, indicating the valence state of Ni in both catalysts is +2, which is consistent with the XPS results. In

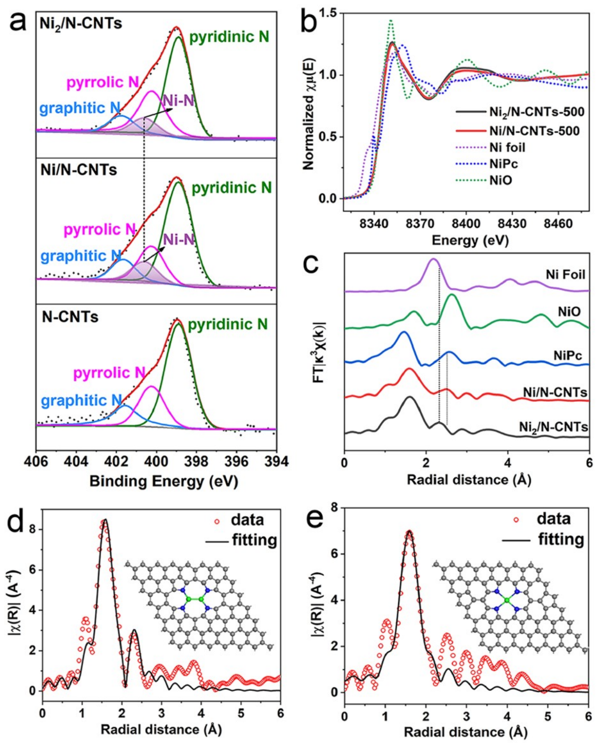

Figure 2 (Color online) (a) High-resolution XPS patterns of N 1s for Ni_2/N-CNTs, Ni/N-CNTs and N-CNTs. (b) Ni K-edge XANES profiles, and (c) FT-EXAFS spectra at R space for Ni_2/N-CNTs, Ni/N-CNTs, NiPc, NiO, and Ni foil. (d, e) The first shell (Ni–N and Ni–Ni) fitting of FT-EXAFS for Ni_2/N-CNTs (d), and Ni/N-CNTs (e) in R space (inset: proposed model for Ni_2/N-CNTs and Ni/N-CNTs catalysts).

contrast, the positions of the absorption threshold for Ni_2/N-CNTs-1000 and Ni/N-CNTs-1000 are between Ni foil and NiO (Figure S12a), indicating the valence state of Ni is between 0 and +2. The Fourier transformations-extended X-ray fine structure (FT-EXAFS) patterns with the references of Ni foil, NiO and NiPc were described in Figure 2c. The primary peak at 1.59 Å in both Ni_2/N-CNTs and Ni/N-CNTs can be assigned to the Ni–N coordination, and this peak position is even longer than the Ni–N distance (1.49 Å) in NiPc due to the weaker coordination of pyrrolic-N. In contrast, the Ni–N distance of 1.38 Å in Ni_2/N-CNTs-1000 and Ni/N-CNTs-1000 is shorter than that of NiPc (Figure S12b) due to the stronger coordination of Ni–$N_{pyridinic}$ compared with that of Ni–$N_{pyrrolic}$, being consistent with the results of XPS measurements. The above results indicate the isolated Ni atoms are coordinated to pyrrolic-N in Ni_2/N-CNTs and Ni/N-CNTs, while they are coordinated to pyridinic-N in Ni_2/N-CNTs-1000 and Ni/N-CNTs-1000. Notably, a small peak at 2.30 Å can be observed in Ni_2/N-CNTs, this distance is close to those of 2.4–2.5 Å observed in the HAADF-STEM image (Figure 1c), and is between the Ni–Ni distance in Ni foil (2.18 Å) and NiO (2.63 Å), demonstrating the Ni–Ni coordination within directly bonded Ni_2 dual-atom pair rather than Ni or NiO nanoparticles in Ni_2/N-CNTs, excluding the existence of metallic Ni or NiO nanoparticles in Ni_2/N-CNTs. In Ni/N-CNTs, a small peak at 2.49 Å, which is close to that of NiPc (2.57 Å), can be assigned to the second Ni–C shell.

The atomic-scale structures of Ni_2/N-CNTs, Ni/N-CNTs, Ni_2/N-CNTs-1000, and Ni/N-CNTs-1000 can be further revealed by the least-squares EXAFS curve fitting, and both the first and the second coordination shells were taken into the analysis in $\chi(R)$ space spectra fitting, and the fitting parameters are summarized in Table S2. For Ni/N-CNTs, the Ni–N coordination number is close to 4.0, suggesting that the isolated Ni atoms are coordinated to four pyrrolic-N atoms in Ni/N-CNTs (Figure 2e, inset). For Ni_2/N-CNTs, the Ni–N/O coordination number is 2.2 in the first shell, and the Ni–Ni coordination number of second shell corresponding to Ni–Ni coordination is 1.0. Based on the above fitting parameters, as well as the XPS and XAS results, a rational structure of Ni_2/N-CNTs was proposed (Figure 2d, inset), in which each Ni atom is coordinated to two pyrrolic-N atoms and one Ni atom. To our knowledge, pyrrolic-N coordinated dual-atom catalyst has not been reported so far. For both Ni_2/N-CNTs-1000 and Ni/N-CNTs-1000, the Ni–N coordination number is close to 4.0 (Table S2), suggesting that the Ni_2 dual-atom sites in Ni_2/N-CNTs was transformed to isolated Ni atoms in Ni_2/N-CNTs-1000 at high pyrolysis temperature. Thus Ni_2/N-CNTs-1000 and Ni/N-CNTs-1000 possess the same structure, in which the isolated Ni atoms are coordinated to four pyridinic-N atoms (Figure S12c, d, inset), which is consistent with the result of HAADF-STEM image (Figure S7c).

The performances of CO_2 reduction reaction (CO_2RR) for as-synthesized catalysts were evaluated in Ar- and CO_2-saturated 0.5 M $KHCO_3$ electrolyte, in a three electrode H-cell separated by a Nafion 117 membrane. Figure 3a and Figure S13 show the linear sweep voltammetry (LSV) curves of Ni_2/N-CNTs, Ni/N-CNTs, Ni_2/N-CNTs-1000, Ni/N-CNTs-1000, and N-CNTs, in which the onset potentials of CO_2 reduction for Ni_2/N-CNTs and Ni/N-CNTs are lower than those of Ni_2/N-CNTs-1000 and Ni/N-CNTs-1000 (Figure S13a), and the catalytic current densities of Ni_2/N-CNTs and Ni/N-CNTs are also obviously higher than those of Ni_2/N-CNTs-1000 and Ni/N-CNTs-1000 from −0.5 to −1.3 V (vs. reversible hydrogen electrode (RHE)), demonstrating the catalytic activity of pyrrolic-N coordinated Ni^{2+} site is much higher than that of pyridinic-N coordinated $Ni^{(0\text{–}+2)}$ site. Moreover, the CO_2RR performance for dinuclear Ni_2L_2 complex and Ni_2L_2/CNTs was also evaluated. As shown in Figure S14, almost no CO was detected, indicating Ni_2L_2 and Ni_2L_2/CNTs are inactive for CO_2RR.

Potentiostatic electrolysis was conducted to evaluate the Faradaic efficiencies (FEs) of the catalysts. The results show that CO and H_2 are the only gas products (Figure S15), and no liquid products were detected by ^{1}H nuclear magnetic

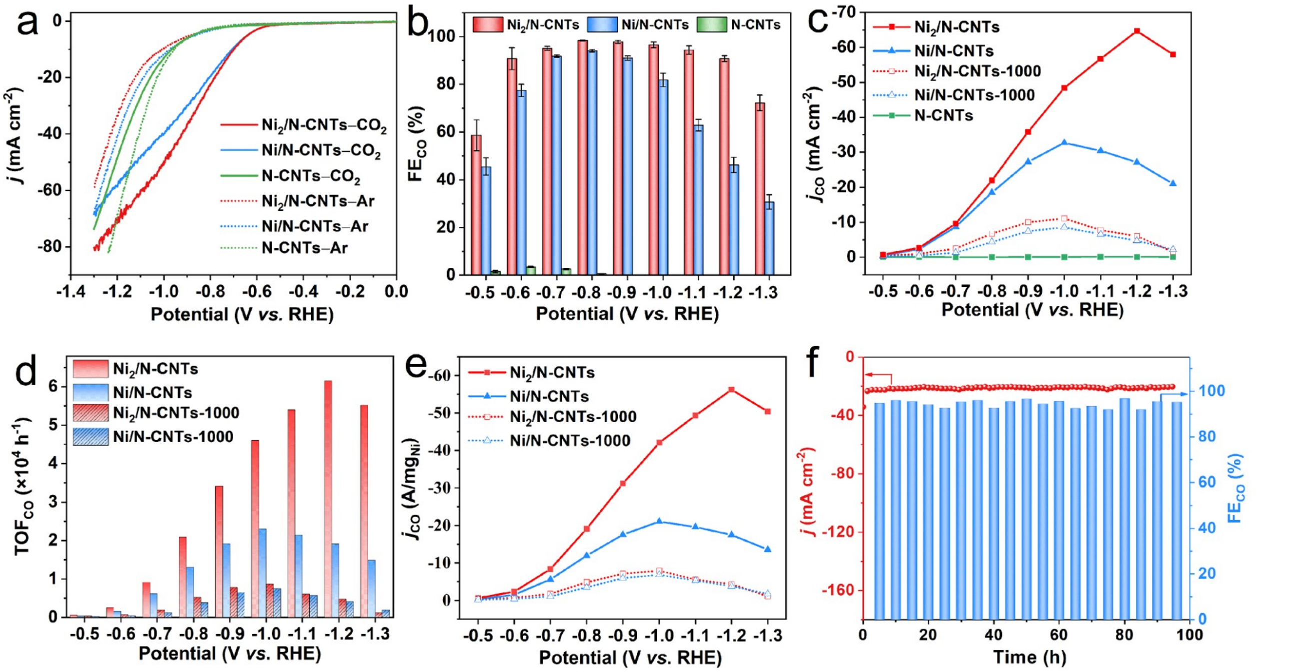

Figure 3 (Color online) (a) The LSV curves of Ni_2/N-CNTs, Ni/N-CNTs and N-CNTs measured in Ar- and CO_2-saturated 0.5 M $KHCO_3$ electrolyte. (b) FE_{CO}, and (c) j_{CO} of Ni_2/N-CNTs, Ni/N-CNTs, Ni_2/N-CNTs-1000, Ni/N-CNTs-1000 and N-CNTs. (d) TOFs of Ni_2/N-CNTs, Ni/N-CNTs, Ni_2/N-CNTs-1000 and Ni/N-CNTs-1000 at various applied potentials. (e) j_{CO} normalized to A/mg_{Ni}. (f) Long-term stability test of Ni_2/N-CNTs at −0.8 V for 96 h.

resonance (NMR) spectroscopy (Figure S16). The calculated Faradaic efficiencies of CO (FE_{CO}) for Ni_2/N-CNTs, Ni/N-CNTs, Ni_2/N-CNTs-1000, Ni/N-CNTs-1000 and N-CNTs are presented in Figure 3b and Figure S13b, respectively. From Figure 3b it can be found that N-CNTs are almost inactive for CO_2RR with poor CO selectivity. For Ni/N-CNTs, the FE_{CO} depends greatly on the applied potentials, and the FE_{CO} reaches a maximum value of 94.7% at −0.8 V. In contrast, Ni_2/N-CNTs exhibits outstanding CO_2RR selectivity in a broad potential window from −0.6 to −1.2 V, giving a maximum FE_{CO} of 98.4 % at −0.8 V. Moreover, the FE_{CO} of Ni_2/N-CNTs-1000 and Ni/N-CNTs-1000 are lower than those of Ni_2/N-CNTs and Ni/N-CNTs (Figure S13b), indicating both the activity and selectivity of pyridinic-N coordinated Ni catalysts are poorer than those of pyrrolic-N coordinated Ni catalysts.

Figure 3c shows the partial current density of CO (j_{CO}) at various potentials. The j_{CO} of Ni_2/N-CNTs is the highest among the five catalysts at all the applied potentials, reaching a maximum j_{CO} value of 64.5 mA/cm^2 at −1.2 V, which is 2.0-, 5.8-, and 7.5-fold higher than the maximum j_{CO} values of 32.6, 11.1 and 8.6 mA/cm^2 at −1.0 V for Ni/N-CNTs, Ni_2/N-CNTs-1000 and Ni/N-CNTs-1000, respectively (Figure 3c), and also larger than those of most reported state-of-the-art DACs (Table S3). The Tafel slope of Ni_2/N-CNTs was calculated to be 178.3 mV/dec, which is smaller than those of Ni/N-CNTs (205.4 mV/dec), Ni_2/N-CNTs-1000 (313.7 mV/dec), and Ni/N-CNTs-1000 (328.4 mV/dec), indicating the enhanced CO_2RR kinetics of Ni_2/N-CNTs (Figure S17). Moreover, the results of electrochemical impedance spectroscopy (EIS) analysis show that Ni_2/N-CNTs possesses the lowest charge-transfer resistance among all the five catalysts (Figure S18), which provides the fastest charge-transfer during the CO_2RR process. For reasonable comparison of the catalytic activity of Ni_2/N-CNTs with those of Ni/N-CNTs, Ni_2/N-CNTs-1000, and Ni/N-CNTs-1000, the mass-normalized j_{CO} values (A/mg_{Ni}) were conducted. As shown in Figure 3e, the j_{CO} mass activity of Ni_2/N-CNTs is also higher than those of Ni/N-CNTs, Ni_2/N-CNTs-1000, and Ni/N-CNTs-1000 at all the applied potentials, with a maximum j_{CO} of 56.2 A/mg_{Ni} at −1.2 V, 2.7-, 7.1-, and 8.3-times higher than the those of 21.1, 7.9 and 6.8 A/mg_{Ni} at −1.0 V for Ni/N-CNTs, Ni_2/N-CNTs-1000, and Ni/N-CNTs-1000, respectively. Considering both the synthesis procedure and the N-CNTs support are identical for Ni_2/N-CNTs and Ni/N-CNTs, the enhanced catalytic activity and selectivity for Ni_2/N-CNTs DAC should originate from the synergistic catalysis within pyrrolic-N coordinated Ni_2 dual-atom sites in Ni_2/N-CNTs.

It is worthy to note that the j_{CO} mass activity of Ni_2/N-CNTs-1000 is close to that of Ni/N-CNTs-1000 (Figure 3e), indicating there is almost no synergistic catalysis in Ni_2/N-CNTs-1000, which is consistent with the result of HAADF-STEM image that the isolated Ni_2 dual-atom sites in Ni_2/N-CNTs were transferred to Ni single-atom in Ni_2/N-CNTs-1000 under high pyrolysis temperature. The lower j_{CO} mass activity of Ni/N-CNTs-1000 than that of Ni/N-CNTs implies that the electrocatalytic performance of pyridinic-N coordinated SACs is lower than that of pyrrolic-N coordinated SACs.

The turnover frequencies (TOF_{CO}) for CO production based on metal sites in Ni_2/N-CNTs and Ni/N-CNTs were calculated to further disclose the intrinsic activity. As shown in Figure 2d, Ni_2/N-CNTs possesses much higher TOF_{CO} than Ni/N-CNTs, Ni_2/N-CNTs-1000 and Ni/N-CNTs-1000 at all the applied potentials, reaching a maximum TOF_{CO} value of 6.2×10^4 h^{-1} at −1.2 V, 2.7-, 7.1-, and 8.3-times higher than those of 2.3×10^4 h^{-1}, 8.6×10^3 h^{-1}, and 7.5×10^3 h^{-1} at −1.0 V for Ni/N-CNTs, Ni_2/N-CNTs-1000 and Ni/N-CNTs-1000, respectively, and it is also higher than those of the most reported state-of-the-art DACs (Table S3). To further reveal the active site for CO_2RR in Ni_2/N-CNTs, the poison experiment was conducted by adding SCN^- in the electrolyte. As shown in Figure S19, the current density was significantly suppressed after introducing SCN^-, demonstrating the dual-site Ni center is the main active site for CO_2RR. Except catalytic current density and selectivity, stability of the catalysts is also important for practical applications. From Figure 3f it can be found that Ni_2/N-CNTs exhibits outstanding durability over 96 h of continuous electrolysis at −0.8 V, with FE_{CO} and current density remaining almost unchanged. The XRD patterns (Figure S20), the SEM and TEM images (Figure S21) of Ni_2/N-CNTs before and after electrolysis are almost identical. Moreover, the results of ICP-MS measurement of Ni_2/N-CNTs indicates that the Ni content after electrolysis is equal to that before electrolysis, indicating no Ni ion leaching during the electrolysis process. All the above results demonstrate the high stability of Ni_2/N-CNTs during CO_2RR process.

The current density of CO_2RR in H-cell is always inherently limited by the mass transfer due to the low solubility of CO_2 in aqueous electrolyte. Therefore, the CO_2RR performance of Ni_2/N-CNTs was evaluated in a flow cell with a gas diffusion electrode (Figure S22a). As shown in Figure S22b, the current density of Ni_2/N-CNTs in the flow cell is far greater than that in the H-cell, with over 90% FE_{CO} in a wide potential range from −0.4 to −0.9 V, and a maximum FE_{CO} of 98.3% at −0.6 V (Figure S22c). Ni_2/N-CNTs delivers a j_{CO} of 206.2 mA/cm^2 at −0.9 V in the flow cell, 6-times higher than that in the H-cell. In addition, Ni_2/N-CNTs shows a stable current density of 100 mA/cm^2 for at least 24 h (Figure S22d), without obvious attenuation of the current density and FE_{CO}, indicating the high stability of the catalyst under high current density in the flow cell.

To further understand the origin of superior electrocatalytic activity of pyrrolic-N coordinated catalysts, the first derivative cyclic voltammetry were performed. From Figure S23 it can be found that obvious reduction peaks were observed at −0.27, −0.34, −0.47, and −0.42 V for Ni_2/N-CNTs, Ni/N-CNTs, Ni_2/N-CNTs-1000 and Ni/N-CNTs-1000, respectively. Previous investigations demonstrate the Ni^{2+} in NiPc, NiPc-CN and NiPc-OM can be partially reduced at −0.68, −0.37 and −0.72 V respectively identified by *in situ* XANES spectra [9], in which the electron-withdrawing CN groups in NiPc-CN can decrease the electron density of Ni site for facilitating the formation a reduced catalytic site to enhance its electrocatalytic activity. Similar phenomenon has also been observed in CoPc-CN molecular catalyst with electron-withdrawing CN group anchored on CNTs [45]. Based on the above results, we can reasonably assign the reduction peaks at −0.27–−0.47 V to partial reduction of Ni(II) to Ni(I), and the significant positive shift of Ni(II)/Ni(I) potentials in Ni_2/N-CNTs and Ni/N-CNTs as compared with Ni_2/N-CNTs-1000 and Ni/N-CNTs-1000 renders a higher fraction of Ni(I) sites in Ni_2/N-CNTs and Ni/N-CNTs at low overpotentials. As a result, pyrrolic-N coordinated catalysts displays higher electrocatalytic performance compared to pyridinic-N coordinated catalysts.

DFT calculations were carried out to reveal the origin of superior electrocatalytic activity of Ni_2/N-CNTs. As shown in Figure 4a, the optimized structures of Ni_2/N-CNTs, Ni/N-CNTs, and Ni/N-CNTs-1000 based on the HAADF-STEM, XPS and EXAFS results, are used as the model for the calculations, and the optimized structures for the intermediates on the above three catalysts are shown in Figure S24. For pyridinic-N coordinated Ni/N-CNTs-1000, the reaction free energy for the reduction of CO_2 to *COOH is as high as 1.76 eV, the highest among all the three catalysts, indicating this step is the rate-determining step for CO_2 reduction on Ni/N-CNTs-1000. In contrast, for pyrrolic-N coordinated Ni/N-CNTs, this value is reduced to 1.07 eV. As a result, the electrocatalytic activity of Ni/N-CNTs is much higher than that of Ni/N-CNTs-1000, demonstrating the electrocatalytic CO_2 reduction activity of pyrrolic-N coordinated SACs is superior to that of pyridinic-N coordinated SACs. For Ni_2/N-CNTs, however, though the reaction free energy for the reduction of CO_2 to COOH* is further reduced to 0.19 eV, the release of CO* from Ni_2 dual-atom site becomes the rate-determining step due to the formation of stable CO-adsorbed Ni_2 intermediate of Ni_2/N-CNTs-*CO (Figure S24), with a large CO desorption free energy of 1.66 eV, indicating Ni_2/N-CNTs itself is not an efficient electrocatalyst for CO_2 reduction either. However, the H_2O-adsorbed Ni_2 dual-atom site in Ni_2/N-CNTs-*H_2O can also act as the catalytic site for the CO_2 reduction. As shown in Figure 4b, c, the reaction free energy for the reduction of CO_2 to COOH* on the H_2O-adsorbed Ni_2 dual-atom site is 0.18 eV, which is similar to that on Ni_2/N-CNTs (0.19 eV). Whereas the subsequent CO desorption on the H_2O-adsorbed Ni_2 dual-atom site is only 0.88 eV, this value is much smaller than that on Ni_2/N-CNTs (1.66 eV), indicating the subsequent CO desorption becomes easier. Based on the above results, it is expected that Ni_2/N-CNTs-*H_2O displays the highest electrocatalytic activity for

CO_2 reduction to CO due to its optimized and moderate reaction free energy for both *COOH formation and CO desorption.

To interpret the binding strengths between metal Ni and the adsorbed *COOH intermediate, the crystal orbital Hamilton population (COHP) was calculated to analyze the interaction of Ni–C. As shown in Figure 5, the integrated COHP (ICOHP) was obtained by integrating COHP over all levels up to the Fermi level, which can estimate the bonding strength (the more negative the value of ICOHP, the stronger the bonding strength). The calculated ICOHP for Ni/N-CNTs-1000, Ni/N-CNTs, Ni_2/N-CNTs and Ni_2/N-CNTs-*H_2O is −1.10, −1.26, −1.61 and −1.60 eV, respectively. This result indicates that the bonding strength of Ni–C in the Ni_2 dual-atom site is much stronger than that in the pyrrolic-N coordinated and pyridinic-N coordinated SACs, which implies that the CO_2 can be easily activated on Ni_2/N-CNTs. In addition, the thermal stability of Ni_2/N-CNTs and Ni/N-CNTs were also evaluated by conducting the *ab initio* molecular dynamics (AIMD) simulations. As depicted in Figure S25, Ni_2/N-CNTs and Ni/N-CNTs show excellent thermal stability over 7 ps. During the simulation time, the geometries of Ni_2/N-CNTs and Ni/N-CNTs remain virtually unchanged and show a narrow energy fluctuation. These results show an excellent thermodynamic stability of as-prepared Ni_2/N-CNTs and Ni/N-CNTs.

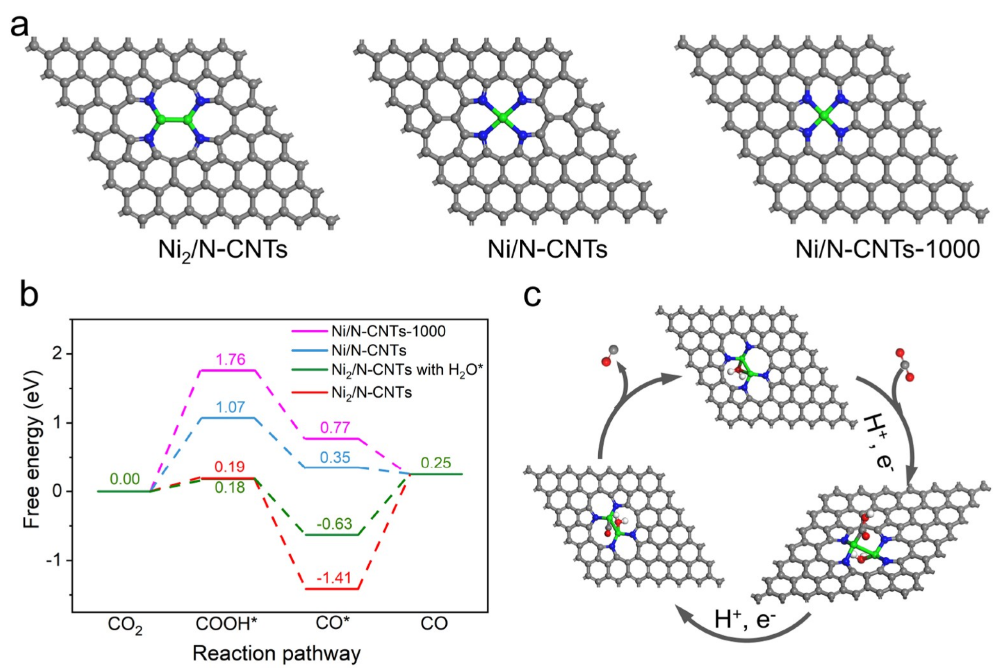

Figure 4 (Color online) (a) The optimized structures of Ni_2/N-CNTs, Ni/N-CNTs, and Ni/N-CNTs-1000 (Ni_2/N-CNTs-1000). (b) Calculated free-energy diagrams for the conversion of CO_2 to CO on different catalysts. (c) The proposed reaction paths of Ni_2/N-CNTs-*H_2O for CO_2 electroreduction to CO.

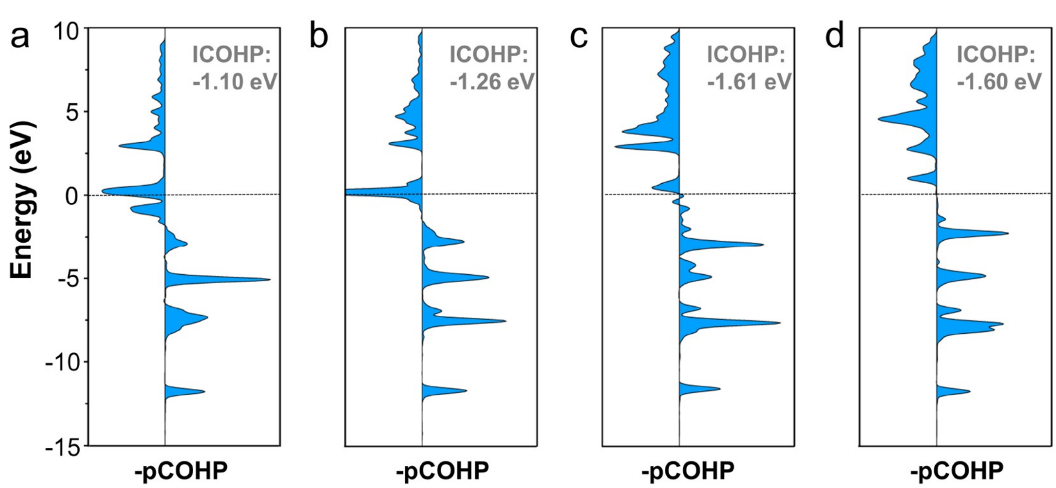

Figure 5 (Color online) The calculated COHP between Ni atom and C atom in *COOH intermediate for (a) Ni/N-CNTs-1000, (b) Ni/N-CNTs, (c) Ni_2/N-CNTs, and (d) Ni_2/N-CNTs-H_2O*.

4 Conclusions

In conclusion, two pyrrolic-N coordinated dual-atom and single-atom catalysts of Ni_2/N-CNTs and Ni/N-CNTs can be controllably synthesized by pyrolyzing the stable complexes of Ni_2L_2 and NiL_2 with O-CNTs in the presence of dicyandiamide at 500 °C, which can be transformed to pyridinic-N coordinated catalysts of Ni_2/N-CNTs-1000 and Ni/N-CNTs-1000 at 1000 °C. The valence states of nickel in pyrrolic-N and pyridinic-N coordinated catalysts are +2 and 0–+2, respectively. Electrochemical measurements reveal that the catalytic activity and FEs of pyrrolic-N coordinated Ni catalysts are much higher than those of pyridinic-N coordinated Ni catalysts, and Ni_2/N-CNTs display the best catalytic performance. The weak electron donor nature of pyrrolic-N facilitates the generation of a reduced active site for benefiting CO_2 electroreduction. DFT calculations reveal that the reaction free energy for the *COOH formation on pyrrolic-N coordinated Ni catalysts are lower than those on pyridinic-N coordinated Ni catalysts, and a H_2O-adsorbed Ni_2/N-CNT displays the optimized reaction free energy for both *COOH formation and CO desorption, which derive the best catalytic performance. Our results indicate that using stable dinuclear complexes as a precursor benefits to controllably synthesize of highly purified dual-atom catalysts, and low and high pyrolyzing temperature favor to form pyrrolic-N and pyridinic-N coordinated catalysts, respectively. This work not only highlights the effect of different species of doped nitrogen on the catalytic activity of CO_2 electroreduction, but also provides a new route for the development of high performance of electrocatalysts for converting CO_2 to fuels.

Acknowledgements This work was supported by the National Key R&D Program of China (2022YFA1502902) and the National Natural Science Foundation of China (21931007 and 21790052).

Conflict of interest The authors declare that they have no conflict of interest.

Supporting information The supporting information is available online at http://chem.scichina.com and http://link.springer.com/journal/11426. The supporting materials are published as submitted, without typesetting or editing. The responsibility for scientific accuracy and content remains entirely with the authors.

1 Yang S, An H, Arnouts S, Wang H, Yu X, de Ruiter J, Bals S, Altantzis T, Weckhuysen BM, van der Stam W. *Nat Catal*, 2023, 6: 796–806
2 Jin S, Hao Z, Zhang K, Yan Z, Chen J. *Angew Chem Int Ed*, 2021, 60: 20627–20648
3 Su J, Musgrave Iii CB, Song Y, Huang L, Liu Y, Li G, Xin Y, Xiong P, Li MMJ, Wu H, Zhu M, Chen HM, Zhang J, Shen H, Tang BZ, Robert M, Goddard Iii WA, Ye R. *Nat Catal*, 2023, 6: 818–828
4 Yang PP, Gao MR. *Chem Soc Rev*, 2023, 52: 4343–4380
5 Amrillah T, Supandi AR, Puspasari V, Hermawan A, Seh ZW. *Trans Tianjin Univ*, 2022, 28: 307–322
6 Li N, Gao H, Liu Z, Zhi Q, Li B, Gong L, Chen B, Yang T, Wang K, Jin P, Jiang J. *Sci China Chem*, 2023, 66: 1417–1424
7 Birdja YY, Pérez-Gallent E, Figueiredo MC, Göttle AJ, Calle-Vallejo F, Koper MTM. *Nat Energy*, 2019, 4: 732–745
8 Li Q, Fu J, Zhu W, Chen Z, Shen B, Wu L, Xi Z, Wang T, Lu G, Zhu J, Sun S. *J Am Chem Soc*, 2017, 139: 4290–4293
9 Zhang X, Wang Y, Gu M, Wang M, Zhang Z, Pan W, Jiang Z, Zheng H, Lucero M, Wang H, Sterbinsky GE, Ma Q, Wang YG, Feng Z, Li J, Dai H, Liang Y. *Nat Energy*, 2020, 5: 684–692
10 Wu Y, Wu M, Zhu J, Zhang X, Li J, Zheng K, Hu J, Liu C, Pan Y, Zhu J, Sun Y, Xie Y. *Sci China Chem*, 2023, 66: 1997–2003
11 Jin Z, Jiao D, Dong Y, Liu L, Fan J, Gong M, Ma X, Wang Y, Zhang W, Zhang L, Gen Yu Z, Voiry D, Zheng W, Cui X. *Angew Chem Int Ed*, 2024, 63: e202318246
12 Dong J, Liu Y, Pei J, Li H, Ji S, Shi L, Zhang Y, Li C, Tang C, Liao J, Xu S, Zhang H, Li Q, Zhao S. *Nat Commun*, 2023, 14: 6849
13 Gu J, Hsu CS, Bai L, Chen HM, Hu X. *Science*, 2019, 364: 1091–1094
14 Zhao C, Wang Y, Li Z, Chen W, Xu Q, He D, Xi D, Zhang Q, Yuan T, Qu Y, Yang J, Zhou F, Yang Z, Wang X, Wang J, Luo J, Li Y, Duan H, Wu Y, Li Y. *Joule*, 2019, 3: 584–594
15 Koshy DM, Chen S, Lee DU, Stevens MB, Abdellah AM, Dull SM, Chen G, Nordlund D, Gallo A, Hahn C, Higgins DC, Bao Z, Jaramillo TF. *Angew Chem Int Ed*, 2020, 59: 4043–4050
16 Liang S, Jiang Q, Wang Q, Liu Y. *Adv Energy Mater*, 2021, 11: 2101477
17 Li QX, Si DH, Lin W, Wang YB, Zhu HJ, Huang YB, Cao R. *Sci China Chem*, 2022, 65: 1584–1593
18 (a) Wang X, Chen Z, Zhao X, Yao T, Chen W, You R, Zhao C, Wu G, Wang J, Huang W, Yang J, Hong X, Wei S, Wu Y, Li Y. *Angew Chem Int Ed*, 2018, 57: 1944–1948; (b) Shi R, Guo J, Zhang X, Waterhouse GIN, Han Z, Zhao Y, Shang L, Zhou C, Jiang L, Zhang T. *Nat Commun*, 2020, 11: 3028
19 Zheng T, Jiang K, Wang H. *Adv Mater*, 2018, 30: 1802066
20 Yang HB, Hung SF, Liu S, Yuan K, Miao S, Zhang L, Huang X, Wang HY, Cai W, Chen R, Gao J, Yang X, Chen W, Huang Y, Chen HM, Li CM, Zhang T, Liu B. *Nat Energy*, 2018, 3: 140–147
21 Ju W, Bagger A, Hao GP, Varela AS, Sinev I, Bon V, Roldan Cuenya B, Kaskel S, Rossmeisl J, Strasser P. *Nat Commun*, 2017, 8: 944
22 Ren W, Tan X, Yang W, Jia C, Xu S, Wang K, Smith SC, Zhao C. *Angew Chem Int Ed*, 2019, 58: 6972–6976
23 (a) Jiao J, Lin R, Liu S, Cheong WC, Zhang C, Chen Z, Pan Y, Tang J, Wu K, Hung SF, Chen HM, Zheng L, Lu Q, Yang X, Xu B, Xiao H, Li J, Wang D, Peng Q, Chen C, Li Y. *Nat Chem*, 2019, 11: 222–228; (b) Zhang S, Gao XT, Hou PF, Zhang TR, Kang P. *Rare Met*, 2021, 40: 3117–3124
24 Hao Q, Zhong H, Wang J, Liu K, Yan J, Ren Z, Zhou N, Zhao X, Zhang H, Liu D, Liu X, Chen L, Luo J, Zhang X. *Nat Synth*, 2022, 1: 719–728
25 Pei J, Yang L, Lin J, Zhang Z, Sun Z, Wang D, Chen W. *Angew Chem Int Ed*, 2024, 63: e202316123
26 Xiao M, Zhang H, Chen Y, Zhu J, Gao L, Jin Z, Ge J, Jiang Z, Chen S, Liu C, Xing W. *Nano Energy*, 2018, 46: 396–403
27 Jiao J, Yuan Q, Tan M, Han X, Gao M, Zhang C, Yang X, Shi Z, Ma Y, Xiao H, Zhang J, Lu T. *Nat Commun*, 2023, 14: 6164
28 Zhu W, Zhang L, Liu S, Li A, Yuan X, Hu C, Zhang G, Deng W, Zang K, Luo J, Zhu Y, Gu M, Zhao ZJ, Gong J. *Angew Chem Int Ed*, 2020, 59: 12664–12668
29 Ouyang T, Huang HH, Wang JW, Zhong DC, Lu TB. *Angew Chem Int Ed*, 2017, 56: 738–743
30 Ouyang T, Wang HJ, Huang HH, Wang JW, Guo S, Liu WJ, Zhong DC, Lu TB. *Angew Chem Int Ed*, 2018, 57: 16480–16485
31 Ding T, Liu X, Tao Z, Liu T, Chen T, Zhang W, Shen X, Liu D, Wang S, Pang B, Wu D, Cao L, Wang L, Liu T, Li Y, Sheng H, Zhu M, Yao T. *J Am Chem Soc*, 2021, 143: 11317–11324
32 Zhang S, Wu Y, Zhang YX, Niu Z. *Sci China Chem*, 2021, 64: 1908–1922
33 Lu Z, Wang B, Hu Y, Liu W, Zhao Y, Yang R, Li Z, Luo J, Chi B, Jiang Z, Li M, Mu S, Liao S, Zhang J, Sun X. *Angew Chem Int Ed*,

2019, 58: 2622–2626
34 Yang Y, Qian Y, Li H, Zhang Z, Mu Y, Do D, Zhou B, Dong J, Yan W, Qin Y, Fang L, Feng R, Zhou J, Zhang P, Dong J, Yu G, Liu Y, Zhang X, Fan X. *Sci Adv*, 2020, 6: eaba6586
35 Geldard JF, Lions F. *J Org Chem*, 1965, 30: 318–319
36 Keij FS, de Graaff RAG, Haasnoot JG, Oosterling AJ, Pedersen E, Reedijk J. *J Chem Soc Chem Commun*, 1988, 423–425
37 Sun Q, Ren W, Zhao Y, Zhao C. *Chem Commun*, 2021, 57: 1514–1517
38 Zhu M, Chen J, Guo R, Xu J, Fang X, Han YF. *Appl Catal B-Environ*, 2019, 251: 112–118
39 Zhao Y, Yang KR, Wang Z, Yan X, Cao S, Ye Y, Dong Q, Zhang X, Thorne JE, Jin L, Materna KL, Trimpalis A, Bai H, Fakra SC, Zhong X, Wang P, Pan X, Guo J, Flytzani-Stephanopoulos M, Brudvig GW, Batista VS, Wang D. *Proc Natl Acad Sci USA*, 2018, 115: 2902–2907
40 Lang R, Xi W, Liu JC, Cui YT, Li T, Lee AF, Chen F, Chen Y, Li L, Li L, Lin J, Miao S, Liu X, Wang AQ, Wang X, Luo J, Qiao B, Li J, Zhang T. *Nat Commun*, 2019, 10: 234
41 Kabir S, Artyushkova K, Serov A, Kiefer B, Atanassov P. *Surf Interface Anal*, 2016, 48: 293–300
42 Serov A, Artyushkova K, Atanassov P. *Adv Energy Mater*, 2014, 4: 1301735
43 Lu P, Zhang J, He H, Wang M, Luo Z, Gao D, Liu Z, Wang X, Yuan M, Dipazir S, Zhao H, Xie Y, Zhang G. *J Power Sources*, 2020, 449: 227496
44 Zhu Z, Yin H, Wang Y, Chuang CH, Xing L, Dong M, Lu YR, Casillas-Garcia G, Zheng Y, Chen S, Dou Y, Liu P, Cheng Q, Zhao H. *Adv Mater*, 2020, 32: 2004670
45 Zhang X, Wu Z, Zhang X, Li L, Li Y, Xu H, Li X, Yu X, Zhang Z, Liang Y, Wang H. *Nat Commun*, 2017, 8: 14675